Accepted Manuscript

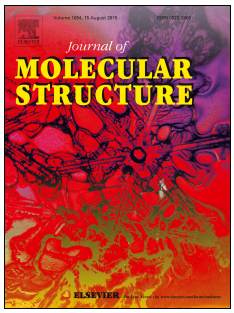

Synthesis, characterization and theoretical study in gaseous and solid phases of the imine 4-Acetyl-*N*-(4-methoxybenzylidene)aniline

J.F.N. Batista, J.W. Cruz, Jr., A.C. Doriguetto, C. Torres, E.T. de Almeida, I. Camps

PII: S0022-2860(17)30843-8

DOI: 10.1016/j.molstruc.2017.06.062

Reference: MOLSTR 23948

To appear in: *Journal of Molecular Structure*

Received Date: 6 June 2016

Revised Date: 6 June 2017

Accepted Date: 14 June 2017

Please cite this article as: J.F.N. Batista, J.W. Cruz Jr., A.C. Doriguetto, C. Torres, E.T. de Almeida, I. Camps, Synthesis, characterization and theoretical study in gaseous and solid phases of the imine 4-Acetyl-*N*-(4-methoxybenzylidene)aniline, *Journal of Molecular Structure* (2017), doi: 10.1016/j.molstruc.2017.06.062.

Synthesis, characterization and theoretical study in gaseous and solid phases of the imine 4-Acetyl-N-(4-methoxybenzylidene)aniline

J.F.N. Batista, J.W. Cruz Jr., A.C. Doriguetto, C. Torres, E.T. de Almeida

Instituto de Química. Universidade Federal de Alfenas - Unifal-MG, Rua Gabriel Monteiro da Silva, 700, CEP 37130-000, Alfenas, MG, Brazil

I. Camps

Laboratório de Modelagem Computacional - La*Model, Instituto de Ciências Exatas. Universidade Federal de Alfenas - Unifal-MG, Rua Jovino Fernades Sales, 2600, CEP 37130-000, Alfenas, MG, Brazil*

Abstract

In the present paper we describe the synthesis and characterization of the Schiff's base or imine 4-Acetyl-N-(4-methoxybenzylidene)aniline **(1)**, which provided experimental support for the theoretical calculations. The imine was characterized by infrared spectroscopy and single crystal XRD techniques. The computational studies were performed using the density functional theory (DFT) for the gaseous and solid phases. As similar compounds already shown biological activity, the pharmacokinetic properties of **(1)** were evaluated. Our results shown that **(1)**, in its gaseous form, it is electronically stable and has pharmacological drug like properties. Due to its structural similarity with commercial drugs, it is a promise candidate to act as a nonsteroidal anti-inflammatory and to treat dementia, sleep disorders, alcohol dependence, and psychosis. From the solid state calculations we obtain that **(1)** is a low gap semiconductor and can act as an absorber for electromagnetic radiations with energy greater that $\sim 0.9\ eV$.

Keywords: Schiff's base, ab initio calculations, electronic structure, ADME properties

1. Introduction

Nitrogenated compounds obtained by condensation reaction of primary amines and aldehydes are called Schiff's base or imines and have a characteristic C=N double bond, where the nitrogen atom is bonded to an aryl or alkyl group. Imines play an important role in Coordination Chemistry due to the formation of stable complexes with transition metals [1]. In our recent papers, several nitrogenated ligands, mainly imines, are employed coordinating to the metal center, such as palladium(II), in order to obtain new complex species with antitumour [2], tuberculostatic [3; 4] and leishmanicidal activities [5].

Computational methods are widely used in material science [6] and in drug development [7] to simulate and predict physical and chemical relevant properties. In material science, properties like electron density, electrostatic potential, electronic orbitals and lower energy conformer (for isolated molecules) and electronic bands and crystal energy (for periodical systems) are among the successfully predicted properties [6]. In drug development process, the quantitative structure activity relationship and the absorption, distribution, metabolism and excretion (ADME) properties are some predicted properties [7].

Due to its wide variety of applications [8; 9], Schiff's base form an important class of organic compounds. In the literature, several computational studies of imines that could aid the design and development of new drugs, the understanding of the coordination geometry and electronic properties of isolated and complexes Schiff's base have been performed [10–14].

The aim of this work is to present an experimental and theoretical study of the title compound (see Fig. 1 for a 2D diagram). The paper is organized as follows. The experimental details are presented in section 2. The theoretical methodology and tools are described in section 3. In section 4, the discussion of the results for the gaseous and solid phase of **(1)** are presented. Our conclusions are summarized in section 5.

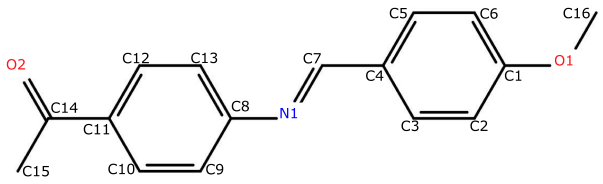

Figure 1: 2D structure diagram. Chemical Abstracts Service (CAS) registry number: 23596-02-3.

2. Experimental methodology

2.1. Synthesis

The materials commercially available were used without purification. The synthesis of the title imine **(1)** was carried out at room temperature. This compound was prepared as described: to a solution containing p-acetophenoneamine 1.2014 g (0.01 mol) and 30.0 mL of ethanol, 1.3614 g (0.01 mol) of p-anisaldehyde was added. The resulting solution was stirred for 8 h and then concentrated under reduced pressure. Distilled water was added and a white solid was formed. The solid was filtered off, washed thoroughly with diethyl ether and water and dried in vacuum. Yield: 90%, mp: 125 ^oC.

2.2. Infrared Spectroscopy

Infrared (IR) spectrum was recorded on a SHIMADZU Prestige 21 FTIR spectrophotometer. The spectrum of **(1)**, in the form of KBr pellets, was recorded in the region $4000 - 400\ cm^{-1}$.

2.3. Single crystal X-ray diffraction

Suitable crystals of **(1)** were grown by slow lower the temperature in the ethanol. Intensity data were measured with the crystal at room temperature (298 K) using the Enraf-Nonius Kappa-CCD diffractometer monochromated by graphite, with MoK_α radiation ($\lambda = 0.71073\ \AA$). The cell refinements were performed using the software Collect [15] and Scalepack [16] and the final cell parameters were obtained on all reflections. Data reduction was carried out using the software Denzo-SMN and Scalepack [16]. The structure

was solved and refined using the software SHELXS97 and SHELXL97, respectively [17]. Non-hydrogen atoms of the molecules were unambiguously solved and full-matrix least-squares refinement of these atoms with anisotropic thermal parameters was carried on. The H atoms were located from the difference electron density synthesis and allowed to ride on their parent atoms, with CH(aromatic)= 0.95 $\AA$ and CH(aliphatic)= 0.97 $\AA$ and $U_{iso}(H) = 1.5U_{eq}$ for methyl H atoms or $1.2U_{eq}$ for the remaining H atoms. Tables were generated by WinGX [18] and the structure representations by ORTEP-3 [18] and Mercury [19]. The intramolecular parameters were analyzed using Mogul [20], a knowledge database of molecular geometry derived from Cambridge Structural Database CSD [21], which provides access to information on the ideal values of bond lengths, valence angles and acyclic torsion angles of similar molecular fragments.

3. Theoretical methodology

To study the structural and electronic properties of the isolated molecule (gaseous phase) we performed quantum mechanics calculations. These calculations were carried out with the *ab initio* density functional theory (DFT) methodology [22–24] together with the 6-311++G** basis-set considering both polarization (**) and diffuse (++) functions and the B3LYP exchange-correlation functional [25] as implemented in the Jaguar package [26]. As input, the molecular geometry determined by the X-ray diffraction analysis (see section 2.3 for details) was used and then optimized. As this conformation is not necessary in the lower energy conformation, all properties presented here were calculated over the optimized structure.

Using the Janak' s theorem [27] it is possible to estimate the chemical potential (μ), the molecular hardness (η) [28] and the electrophilicity index (ω) [29] from the HOMO and LUMO energies ϵ_H and ϵ_L, respectively as following:

$$\mu \cong \frac{\epsilon_L + \epsilon_H}{2} \tag{1}$$

$$\eta \cong \frac{\epsilon_L - \epsilon_H}{2} \tag{2}$$

$$\omega = \frac{\mu^2}{2\eta} \tag{3}$$

To determine the ADME properties the simulations were done with the QikProp software [30]. When performing an evaluation, QikProp quickly analyzes the type of atoms and its charges, and angles, volume and surface area of the molecule. QikProp then uses these information together with the calculated physical descriptors, using Monte Carlo statistical mechanics in the regression equations and semi-empirical calculations. The result is a precise prediction of the pharmacologically relevant properties of a molecule.

To study the structural and electronic properties of the solid phase, the calculations were done considering the DFT methodology for periodical systems [24; 31]. In the case of organic molecular crystals, one of the main interaction that maintain the cohesion of the crystal is the hydrogen interaction [32; 33]. This type of non-chemically bonded, nonlocal and long-ranged interaction is often named as "van der Waals" (vdW) interaction. Until a few years ago, the mostly used DFT approximations implemented in the solid phase simulations software were the local density approximation (LDA) and the generalized gradient approximation (GGA). Since the beginning of the last decade, the first works appear with new approximations including van der Waals dispersion forces [34–39].

We used the software SIESTA [40] together with the van der Waals density functional as proposed by Klimeš *et al.* [36]. Norm conserving Troullier–Martins pseudopotentials [41] were generated with the ATOM software (part of the SIESTA package) to avoid the explicit treatment of the electrons. For the valence electrons, we used a split-valence double-zeta basis set with polarization functions (DZP) [42]. The structure optimizations were done until the Hellman-Feynman forces were below 0.04 $eV\mathring{A}^{-1}$. To obtain results sufficiently accurate, convergence studies were done for the mesh cutoff energy and the number of **k**-points. The total energy convergence for the system was obtained for a mesh cutoff of 300 Ry and for a **k**-point set of $8 \times 8 \times 8$. The Brillouin zone was sampled folowing the

Monkhorst and Pack scheme [43].

To better understand the intermolecular interactions, the use of tables with the interatomic distances is widely used. This methodology is difficult to interpret, suffering of a natural lack of information. Here we decided to use the Hirshfeld surface and fingerprint tools [44–48] to easily visualize and analyze the intermolecular interactions and the packing behavior.

The purpose of the Hirshfeld surface is to define the molecule occupied space in a crystal from the partition of electron density into molecular fragments. Using this idea, a weight function ($w_A(\mathbf{r})$) for a molecule A in a crystal is defined as:

$$w_A(\mathbf{r}) = \rho^{promolecule}(\mathbf{r}) / \rho^{procrystal}(\mathbf{r}), \tag{4}$$

where $\rho^{promolecule}(\mathbf{r})$ is the sum of the electron density over the atoms in the molecule A (promolecule) and $\rho^{procrystal}(\mathbf{r})$ is the sum of the electron density over the crystal (procrystal). The Hirshfeld surface is obtained setting $w_A(\mathbf{r}) = 0.5$.

4. Results and discussion

4.1. Structural properties

The crystal data and refinement parameters are presented in Table 1. Crystallographic data for **(1)** has been deposited in the Cambridge Crystallographic Data Centre as a supplementary publication, CCDC789276.

Figure 2 shows an ORTEP representation of the molecular structure of **(1)**. An overlay of the molecular backbones in both the experimental and the theoretical intramolecular structures of **(1)** clearly shows the conformational similarity between them. The r.m.s. deviation between analogous non-H atoms is 0.015 $\AA$.

The Mogul [20] analysis revealed that all bond lengths correspond with the expected values for a good X-ray diffraction structure refinement. There are two molecular moieties, which are individually almost flat: the moiety 1 containing the atoms O2, C15 and N1

Table 1: Crystal data and structure refinement for **(1)**.

Empirical formula	$C_{16}H_{15}N_1O_2$
Formula weight ($gmol^{-1}$)	253.29
Temperature (K)	298(2)
Wavelength ($\AA$)	0.71069
Crystal system	monoclinic
Space group	$P2_1/c$
Unit cell dimensions:	
a($\AA$)	16.553(5)
b($\AA$)	7.928(5)
c($\AA$)	10.581(5)
β (^{o})	107.727(5)
Volume ($\AA^3$)	1322.6(11)
Z (dimer/cell)	4
$D_{(calc)}$ (Mg/m^3)	1.272
Absorption coefficient (mm^{-1})	0.084
F(000)	536
Crystal size	$0.04 \times 0.21 \times 0.24$ mm^3
Theta range for data collection (^{o})	3.27 to 25.00
Index ranges	$-19 <= h <= 18$, $-9 <= k <= 9$, $-12 <= l <= 11$
Reflections collected	7904
Independent reflections	2325 [R(int) = 0.0443]
Completeness to theta = 0.50^o (%)	0.0
Refinement method	Full-matrix least-squares on F^2
Data / restraints / parameters	2325 / 0 / 172
Goodness-of-fit on F^2	1.024
Final R indices [I>2sigma(I)]	R1 = 0.0485, wR2 = 0.1246
R indices (all data)	R1 = 0.0732, wR2 = 0.1419
Largest diff. peak and hole ($\AA^3$)	0.212 and -0.159

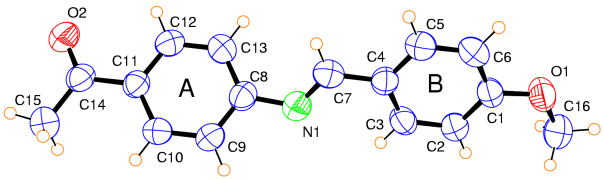

Figure 2: ORTEP representation of **(1)**.

and those ones present in rings A and the moiety 2 containing ring B and N1, O1, C7 and C16. The largest deviations from the least squares plane through the moieties 1 and 2 are $-0.124(2)$ and $-0.054(2)$ $\AA$ for N1 and C7 atoms, respectively. The least squares planes of the moieties 1 and 2 form an angle of $50.52(6)^o$. This geometric feature is also highlighted by the torsional angle considering C7-N1-C8-C13 (torsion= $45.08(1)^o$). The N1 atom, which belongs to both planar moieties, is slightly closer to the moiety 2 ($0.039(1)\AA$) than the moiety 1 ($-0.124(2)\AA$).

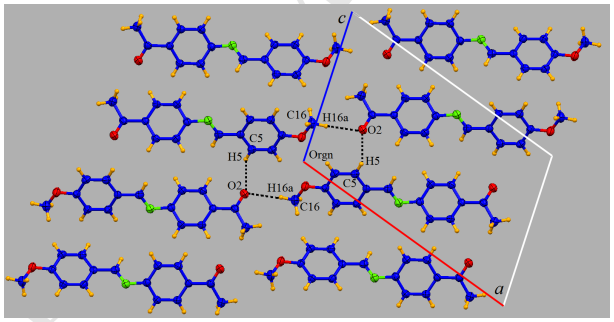

Figure 3: Non-classical hydrogen bonds of **(1)** forming chains along [101] direction.

The supramolecular analysis of **(1)** shows that there are two non-classical hydrogen bonds contributing to the stabilization of the crystal packing (figure 3). Either the C5H5 or C16H16A groups act as intermolecular hydrogen bond donors to the O2, forming a bifurcated hydrogen bond that gives rise to chains along the [101] direction. Parallel chains are linked together by van der Waals interactions forming a infinite two-dimensional network parallel to the plane (010). No significant $\pi - \pi$ interactions is observed and the parallel planar 2D network on the (010) planes are linked along the [010] direction by van

der Waals interactions completing the 3D packing.

Starting from the X-ray structure, it were performed two types of structure optimizations. The first one was done setting the cell parameters fixed and letting the atoms free to move (hereafter called Type-I structure). The second optimization was considering the cell parameters and the atoms free to move (hereafter called Type-II structure). The crystal structure parameters are summarized in Table 2.

Table 2: Crystal parameters as obtained from X-ray analysis and for the optimized crystal.

Parameter	Type-I	Type-II
a ($\AA$)	16.553(5)	15.9987
b ($\AA$)	7.928(5)	7.5556
c ($\AA$)	10.581(5)	9.6178
α	90.0	90.0
β	107.727(5)	103.7432
γ	90.0	90.0
$Volume$ ($\AA^3$)	1322.6(11)	1129.314

From Table 2 we can see that Type-II (full optimized) structure is a more dense structure. The Type-II structure has lower values for the cell parameters and the angles did not present appreciable variations. As a result, the full optimized structure maintain its monoclinic symmetry and the decreased in volume after the optimization gave place to a more compact structure.

The calculated and experimental infrared spectra are shown in Fig. 4. All calculated oscillation frequencies were positive (red ticks in Fig. 4), indicating that a minimum energy optimized structure was reached.

The solid state experimental IR spectrum (upper solid blue line in Fig. 4), shows high intensity bands at 1670 cm^{-1}, assigned to C=N stretch characteristics of the imines or Schiff's base and the bands at 1585 cm^{-1} and 1510 cm^{-1} are assigned to C=C stretches of

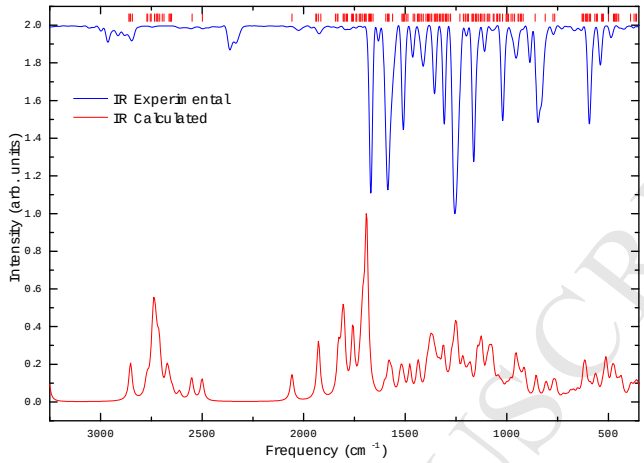

Figure 4: Infrared spectra. Experimental spectrum (upper solid blue line), theoretical spectrum (down solid red line) and calculated frequency positions (red ticks).

the aromatic rings. Two strong bands appears in 831 cm^{-1} and 846 cm^{-1}. These bands are seen in the typical spectrum of para-disubstituted rings present in **(1)**. In the 2800 to 3500 cm^{-1} region, several bands assigned to C-H stretching of the methyl groups appear.

The bands observed at 2330 cm^{-1} and 1700 cm^{-1} are assigned to $\nu(CO)$ from CO_2 and ketonic group, respectively. Also the larger band at 3520 cm^{-1} was assigned to $\nu(OH)$ of water, contaminants hard to eliminate by the KBr pellets technique.

The theoretical spectrum was generated from the calculated peak positions/intensities using Gaussian functions with 100 cm^{-1} width. It is well known that *ab initio* vibrational frequencies are typically larger than the experimental ones [49; 50]. Taking this shift into account, Fig. 4 shows a good correspondence between experimental and calculated IR spectra in the peaks positions. This means that the theoretical methodology used here is suitable to predict the molecular properties.

4.2. ADME properties

In silico predictions of the ADME properties had become a very useful tool decreasing costs in the discovery and development of new drugs. Consequently, eliminating compounds

with high-risk or bad ADME properties earlier in the drug production pathway has become an attractive approach [51]. Alternatively, the ADME properties could guide scientists to suggest modifications based on the structure-activity relationship.

To know the drugability of **(1)**, the ADME properties were simulated using the QikProp software [30]. Some of the most used descriptors are shown in Table 3. As it can be seen, all the parameters are in agreement with the statistically favorable values. It is noteworthy that no violation occurs to the Lipinski's rule of five [52] and Jorgensen's rule of three [53], widely used descriptors in drugability predictions.

Table 3: Some of the calculated ADME properties of compound **(1)**.

Property	*Value*	Recommended
MW[1]	253.300	130.0 – 725.0
QPlogPoct[2]	11.553	8.0 – 35.0
QPlogPw[3]	6.020	4.0 – 45.0
QPlogPo/w[4]	3.259	2.0 – 6.5
QPlogS[5]	-3.993	−6.5 – 0.5
RuleOfFive[6]	0	maximum is 4
RuleOfThree[7]	0	maximum is 3

[1] Molecular weight of the molecule. [2] Predicted octanol/gas partition coefficient. [3] Predicted water/gas partition coefficient. [4] Predicted octanol/water partition coefficient. [5] Predicted aqueous solubility, $logS$. S in $mol \cdot dm^3$ is the concentration of the solute in a saturated solution that is in equilibrium with the crystalline solid. [6] Number of violations of Lipinski's rule of five. [7] Number of violations of Jorgensen's rule of three.

Together with the calculation of ADME descriptors, the QikProp package is able to identify similar drug molecules. In this case, the top 4 compounds with similarity greater that 90% were Melperone® (used to treat dementia, sleep disorders, alcohol dependence

and psychosis), Medifoxamine® (an antidepressant which acts as a dopamine reuptake inhibitor), Fenbufen® and Ketoprofen® both used as nonsteroidal anti-inflammatory drug (NSAID). These results point out **(1)** as a promise candidate for treating these diseases.

4.3. Electronic properties

The highest occupied molecular orbital (HOMO) and the lowest unoccupied molecular orbital (LUMO) are shown in Fig. 5. From the diagram we can see that these orbitals are asymmetrically spread over the entire molecular structure. This is a desirable characteristic for molecular electronic since the device can behave differently with different bias.

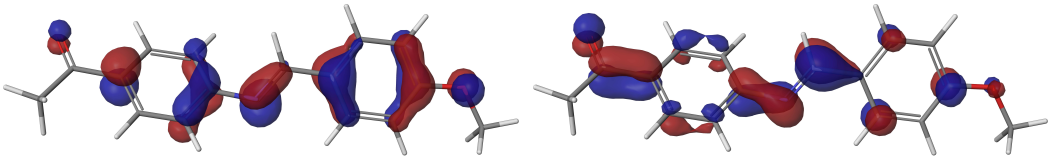

(a) (b)

Figure 5: Molecular orbitals (a) HOMO and (b) LUMO (diagrams rendered with the Maestro software [54]).

The calculated values of chemical potential (μ), the molecular hardness (η) and the electrophilicity index are shown in Table 4. From them, we can infer that as η has a positive value, the redistribution of the electrons in the molecule is energetically unfavorable. Also, the higher η value is, the more stable the molecule is and, therefore, the harder the rearrangement of its electrons [55]. The electrophilicity index, ω, can be used as a measure of the molecule energy lowering due to the maximal electron flow between the environment and the molecule [29]. This is a very useful tool when studying the ligand-binding phenomena in drug design: higher values of ω implies lower energies for the ligand (more stability).

In Fig. 6 the Hirshfeld surface together with the hydrogen interaction for Type-II structure is shown. The figure stands for a mapping of d_{norm} over the Hirshfeld surface. The

Table 4: Calculated parameters ϵ_L, ϵ_H, μ, η and ω.

Property	$Value$(eV)
ϵ_L	-2.183
ϵ_H	-6.221
μ	-4.202
η	2.019
ω	4.372

function d_{norm} represents a symmetric function of distances from the inside and outside of the Hirshfeld surface nuclei (d_i and d_e, respectively), relative to their respective van der Waals radii. The red regions represent distances shorter than vdW separations (highlighting both donor and acceptor equally) whereas white regions represent distance equal to vdW and blue regions for distances greater than vdW. The red spot in Fig. 6 indicate that the van der Waals interactions are the main responsible for the crystal stability and cohesion, therefore a more compact structure.

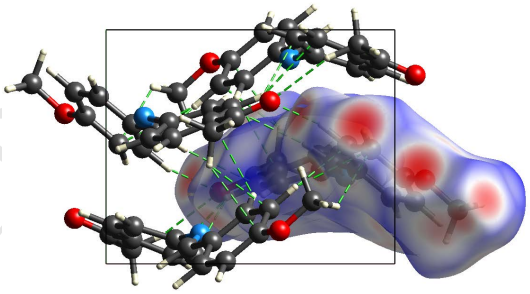

Figure 6: Hirshfeld surface and hydrogen interactions (dashed green lines). Diagram rendered with the *CrystalExplorer* software [56].

Another useful tool to visualize the distribution and type of interactions inside the crystal is the fingerprint plot. The fingerprint plots correspond to 2D histograms for the distribution of (d_i, d_e) pairs from the Hirshfeld surface. In Fig. 7 the calculated fingerprint

plots for Type-II structure are shown.

In Fig. 7a the contributions of all atoms from the molecule are represented. At first sight, it can be seen that the intermolecular contact distribution is bellow 2.2$\AA$. This is in accordance to the fact that Type-II structure is more compact than Type-I were the contact distances extend to more than 2.5$\AA$. The sharp spikes in the plots characterize the hydrogen interactions: longer spikes represent stronger hydrogen bonds, the upper spark corresponds to the hydrogen interaction donor ($d_e > d_i$) and the other one to the hydrogen interaction acceptor ($d_i > d_e$).

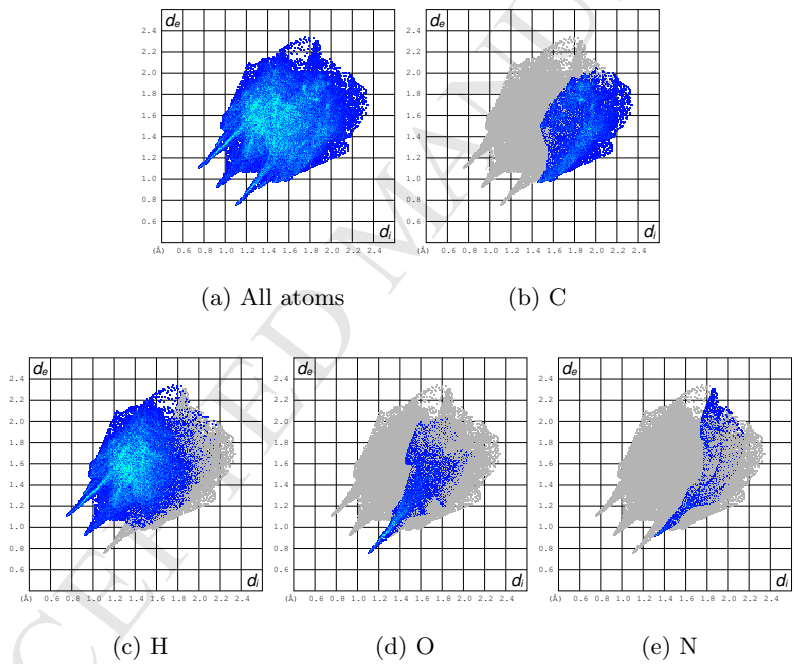

(a) All atoms (b) C

(c) H (d) O (e) N

Figure 7: Fingerprint plots for Type-II structure. Maps for atoms in the promolecule (a) all atoms; (b) carbon atoms; (c) hydrogen atoms; (d) oxygen atoms and (e) nitrogen atoms. Diagrams rendered with the *CrystalExplorer* software [56].

To get a better understanding about what atoms contribute more to the crystal cohesion and how they do that, it is possible to plot the fingerprints for a given type of atom from the promolecule, representing in this way, the interaction of it with all other atoms from

the procrystal. In both structures, the carbon and hydrogen atoms are responsible for more than 80% of the interactions. Their contributions are shown in figures 7b (carbon atoms) and figures 7c (hydrogen atoms). Figure 7d and Fig. 7e shown the contributions of oxygen and nitrogen atoms, respectively. Both atoms behave like hydrogen interaction acceptors.

One of the properties that can be calculated within the quantum mechanical approach is the partial atomic charge distribution. To accomplish this task, there are several methodologies like (i) Mulliken population analysis [57–60], (ii) natural population analysis (NPA) [61], (iii) the Breneman-Wiberg (BW) model [62], (iv) Merz-Kollman-Singh (MKS) electrostatic potential derived charges [63; 64], (v) the Bader partition scheme [65–68], (vi) the Voronoi partition scheme [69; 70] and (vii) the Hirshfeld partition scheme [71]. However, none of them is universally accepted as the "best" for computing partial atomic charges. Here, we decided to use the Hirshfeld partition scheme as it proves to be highly insensitive to the choice of the basis set [71; 72]. In Fig. 8 the calculated charges for Type-II structure are shown.

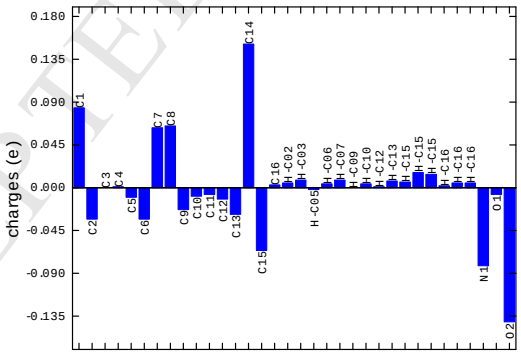

Figure 8: Charge distribution using the Hirshfeld [71] partition scheme for Type-II structure.

In Fig. 9 the calculated total density of states (DOS) together with each atom contribution are shown. The systems did not show spin polarization. The states over the Fermi energy (E_F, dashed green line) are the states available in the conduction band and the

states below the Fermi energy represents the states from the valence bands. As it can be seen, the conduction states are formed mainly with carbon orbitals whereas the valence band states are formed with the contribution of carbon and oxygen orbitals.

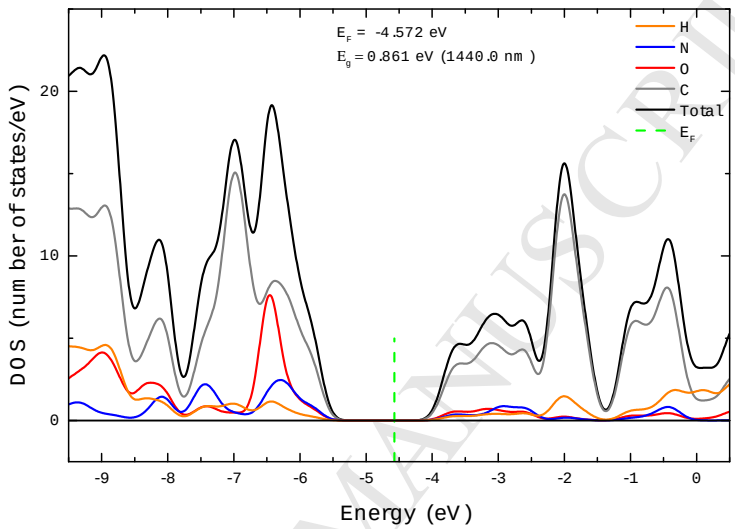

Figure 9: Total density of state (DOS, solid black line) for Type-II structure and individual atoms contributions: carbon (solid gray line), oxygen (solid red line), nitrogen (solid blue line) and hydrogen (solid orange line).

A visible energy gap (E_g) equal to equal to 0.861 eV appears. From an optical point of view, this energy gap implies that **(1)** is transparent for electromagnetic radiation with energies below 0.861 eV and have available states for the absorption of radiation with energies greater that 0.861 eV including part of the infrared region, the visible and ultraviolet regions. These properties indicate that **(1)** can be used as a low gap organic semiconductor very useful in optoelectronic applications.

4.4. Gaseous vs solid

The structural and electronic properties of an isolated molecule (gaseous form) are very different when the same molecule is in its crystal form. This is due to the collective contribution of each molecule and the geometrical restriction imposed by crystal periodicity.

The title compound **(1)**, in its gaseous phase, has the lower possible symmetry (C_1) for a molecule. In its crystal form, the system belongs to the $P2_1/c$ space group, which is also a low–symmetry space group. A low–symmetry system has low geometrical restrictions which are translated in fewer limitations for the physical properties [73].

In table 5, the calculated root–mean–square deviation (RMSD) and maximum distance between two equivalent atoms (MaxD) using the molecule overlay feature of Mercury [19] software is shown for the three structures.

Table 5: Calculated RMSD/MaxD (in $\AA$)

	Gaseous	Type-I	Type-II
Gaseous	0	0.8645/2.2184	0.2919/0.5968
Type-I	0.8645/2.2184	0	0.8460/2.4884
Type-II	0.2919/0.5968	0.8460/2.4884	0

The lower values for the RMSD and MaxD is for the pair gaseous/Type-II structures. This is expected as the Type-II was optimized without any constrains, permitting the full variations of atoms position together with cell parameters.

In Fig. 10 the calculated infrared spectra for the gaseous and solid phases (Type-II structure) are shown.

The infrared spectra of molecules in the gaseous phase are characteristic of a free molecule without any kind of interaction. In the solid phase, the crystalline order has two effects. First, the symmetry of each molecule can be changed due to distortions in its structure owing to the interactions with its nearest neighbors. The second effect is the appearance of new oscillation modes due to the coupling (in-phase or out-of-phase) between neighboring molecules in the crystal unit cell [74].

The oscillation modes of **(1)** in its gaseous phase are concentrated in the regions $1750\,cm^{-1}$ to $250\,cm^{-1}$ and over $3000\,cm^{-1}$. The first region of oscillations is also visible in the spectrum for the solid phase whereas the oscillations in the second region were

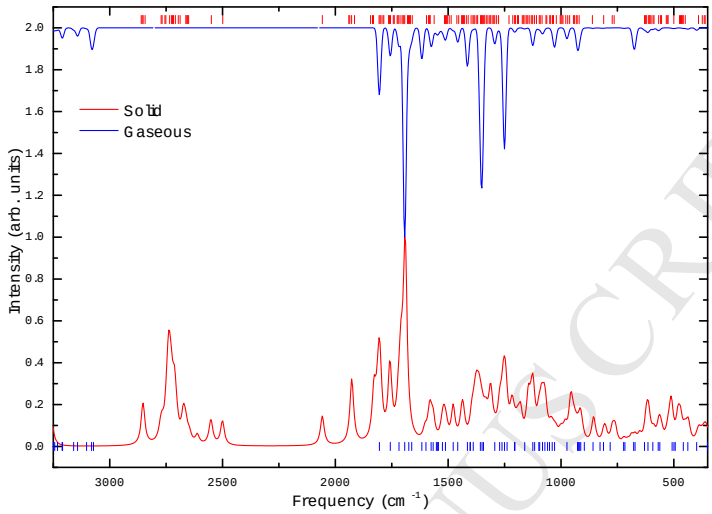

Figure 10: Infrared spectra. Gaseous phase (upper blue lines), solid phase (Type-II structure, down red lines) and calculated frequency positions (ticks).

not reproduced at the solid phase. The appearance of the other bands in the solid phase spectrum were associated with the coupling of the 4 molecules present in the unit cell.

The molecular orbitals of a single molecule are formed from the superposition of atomic orbitals and can be calculated using the linear combinations of atomic orbitals (LCAO) approximation [6]. The results are discrete energy levels. In the solid phase (organic crystals), the overlap of atomic and molecular orbitals produce bands instead discrete energy levels. In this case, the translational symmetry of the crystal gives rise to another quantum number **k** that represents the momentum of the electrons.

The results from the Natural Bond Orbital (NBO) analyzes [75; 76] (using the Canonical Molecular Orbital Composition) for the HOMO and LUMO orbitals are summarized in table 6. The HOMO has significant contributions from at least 9 NBOs whereas the LUMO has a contribution from 6 NBOs. All the participant NBOs has a p character. The results obtained from NBO analysis are in agreement with the orbital distribution (see inset of Fig. 11).

Table 6: Natural bond orbital analysis for HOMO and LUMO

HOMO	LUMO
0.395*[33]: BD(2) C3-C7	0.536*[72]: BD*(2) N2-C5*
0.356*[29]: BD(2) N2-C5	0.373*[90]: BD*(2) C8-O19*
0.337*[42]: BD(2) C6-C11	0.316*[80]: BD*(2) C4-C13*
0.298*[21]: LP(2) O1(lp)	-0.311*[76]: BD*(2) C3-C7*
-0.290*[37]: BD(2) C4-C13	0.273*[68]: LV(1) C14(lv)
0.272*[23]: LP (1) C10(lp)	-0.247*[50]: BD(2) C9-C16
-0.269*[100]: BD*(2) C12-C15*	
0.248*[68]: LV(1) C14(lv)	
0.236*[93]: BD*(2) C9-C16*	

BD: bond, BD*: antibond, LP: lone pair (unfilled valence-shell), LV: lone vacancy (unfilled valence nonbonding).

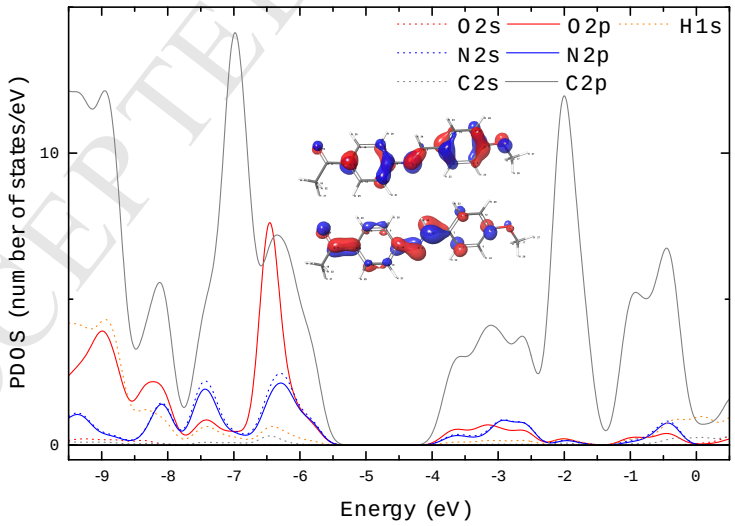

Figure 11: Partial density of states for Type-II system and HOMO/LUMO molecular orbitals.

For the solid state phase, the partial density of states is shown in Fig. 11. As can be seen, the main contributions to the conduction and valence bands are from the carbon atoms. For the valence band, there is also a contribution from the $2p$ orbitals from oxygen and nitrogen atoms.

Comparing both results (table 6 and Fig. 11) it is possible to affirm that the same type of atoms contributes for the HOMO/LUMO and valence/conduction bands, respectively.

5. Conclusions

The structural and electronic properties of compound **(1)** were determined in gaseous and solid phases from experimental and theoretical approaches.

In this case, we obtain a good correspondence between experimental and calculated IR spectra indicating that the theoretical methodology is adequate to simulate the properties of these compound. The calculated molecular hardness (η) and the electrophilicity index (ω) show an electronically stable molecule which is suitable to bind or interact with other chemical species without appreciable electronic modifications. The calculation of ADME properties indicate that **(1)** has drug like properties and from similarity with other commercial drugs, it is a promise candidate to act as a nonsteroidal anti-inflammatory and to treat dementia, sleep disorders, alcohol dependence and psychosis.

For the solid phase, the crystal was grown and its structure was experimentally determined using single crystal X-ray diffraction. Starting with the experimental crystal structure, two structure optimizations were done considering van der Waals dispersion forces, very important in organic crystals. The type of interactions between atoms and their contribution to the crystal cohesion were graphically analyzed using the Hirshfeld surface and fingerprints. The calculated density of states show that **(1)** is a low gap semiconductor and can act as an absorber for electromagnetic radiations with energy greater that $\sim 0.9\ eV$.

6. Acknowledgments

We would like to thank CAPES, CNPq, FINEP, and FAPEMIG (Grant CEX-APQ-01984-14) for financial support. This work is also a collaboration research project of a member of the Rede Mineira de Química (RQ-MG) supported by FAPEMIG (Grant REDE-113/10). Part of the results presented here were developed with the help of CENAPAD-SP (Centro Nacional de Processamento de Alto Desempenho em São Paulo) grant UNICAMP-FINEP-MCT.

The authors express sincere thanks to Prof. Javier Ellena at IFSC (Instituto de Física da USP, São Carlos-SP) for the measurements and support of the X-ray facilities.

[1] X. Wu, M. Tamm, Transition metal complexes supported by highly basic imidazolin-2-iminato and imidazolin-2-imine N-donor ligands, Coord. Chem. Rev. 260 (2014) 116–138.

[2] N. C. CampanellaI, M. da Silva Demartini, C. Torres, E. T. de Almeida, C. M. C. ao Paiva Gouvêa, The cytotoxic and growth inhibitory effects of palladium(II) complexes on MDA-MB-435 cells, Genet. Mol. Biol. 35 (2012) 159–163.

[3] A. C. Moro, A. C. Urbaczek, E. T. de Almeida, F. R. Pavan, C. Q. Leite, A. V. Netto, A. E. Mauro, Binuclear cyclopalladated compounds with antitubercular activity: synthesis and characterization of $[Pd(C^2, N - dmba)(X)\_2(\mu - bpp)](X = Cl, Br, NCO, N\_3$; bpp=1,3-bis(4-pyridyl)propane), J. Coord. Chem. 65 (2012) 1434–1442.

[4] C. G. Oliveira, P. I. da S. Maia, M. Miyata, F. R. Pavan, C. Q. F. Leite, E. T. de Almeida, V. M. Deflon, Cobalt(III) complexes with thiosemicarbazones as potential anti-*Mycobacterium tuberculosis* agents, J. Braz. Chem. Soc. 25 (2014) 1848–1856.

[5] L. P. Franco, E. P. de Góis, B. S. Codonho, A. L. R. Pavan, I. de Oliveira Pereira, M. J. Marques, E. T. de Almeida, Palladium(II) imine ligands cyclometallated complexes with a potential leishmanicidal activity on *Leishmania (L.) amazonensis*, Med. Chem. Res. 22 (2013) 1049–1056.

[6] F. Giustino, Materials Modelling using Density Functional Theory. Properties and Predictions, Oxford University Press, 2014.

[7] S. Ekins, B. Wang (Eds.), Computer Applications in Pharmaceutical Research and Development, Wiley series in drug discovery and development, Wiley Interscience, 2006.

[8] S. Kumar, D. N. Dhar, P. N. Saxena, Applications of metal complexes of Schiff base-A review, J. Sci. Ind. Res. 68 (2009) 181–187.

[9] A. Kajal, S. Bala, S. Kamboj, N. Sharma, V. Saini, Schiff Bases: A versatile pharmacophore, J. Catal. 2013 (2013) 893512.

[10] R. Joseph, J. P. Chinta, C. P. Rao, Lower Rim 1,3-Diderivative of Calix[4]arene-Appended Salicylidene Imine (H_2L): Experimental and Computational Studies of the Selective Recognition of H_2L toward Zn^{2+} and Sensing Phosphate and Amino Acid by [ZnL], J. Org. Chem. 75 (2010) 3387–3395.

[11] A. K. Rochani, B. Suma, S. Kumar, J. Jays, V. Madhavan, QSAR, ADME and QSTR studies of some synthesized anti-cancer 2-indolinone derivatives, Int. J. Pharm. Bio. Sci. 1 (2010) 208–218.

[12] P. Anwar, S. Bobby, Design, docking study and ADME prediction of Chalcone derivatives as potent Tubulin inhibitors, J. Comput. Methods Mol. Des. 4 (2014) 1–5.

[13] M. E. Castro, M. J. Percino, M. Cerón, G. Soriano, V. M. Chapela, Theoretical inhibition efficiency study of Schiff base (E)-2-(2-hydroxybenzylideneamino)phenylarsonic acid and its isomers, Int. J. Electrochem. Sci. 9 (2014) 7890–7903.

[14] N. S. H. N. Moorthy, U. B. Vittal, C. Karthikeyan, V. Thangapandian, A. P. Venkadachallam, P. Trived, Synthesis, antifungal evaluation and *in silico* study of novel Schiff bases derived from 4-amino-5 (3,5-dimethoxy-phenyl)-4H-1,2,4-triazol-3-thiol, Arabian J. Chem. in press.

[15] Nonius [or Hooft, R. W. W.] (1998). COLLECT. Nonius BV, Delft, The Netherlands.

[16] Z. Otwinowski, W. Minor, [20] Processing of X-ray diffraction data collected in oscillation mode , in: J. Charles W. Carter (Ed.), Macromolecular Crystallography Part A, Vol. 276 of Methods in Enzymology, Academic Press, 1997, pp. 307 – 326.

[17] G. M. Sheldrick, A short history of *shelx*, Acta Crystallogr. A 64 (2008) 112–122.

[18] L. J. Farrugia, *WinGX* and *ortep for windows*: an update, J. Appl. Cryst. 45 (2012) 849–854.

[19] C. F. Macrae, P. R. Edgington, P. McCabe, E. Pidcock, G. P. Shields, R. Taylor, M. Towler, J. van de Streek, *Mercury*: visualization and analysis of crystal structures, J. Appl. Cryst. 39 (2006) 453–457.

[20] I. J. Bruno, J. C. Cole, M. Kessler, J. Luo, W. D. S. Motherwell, L. H. Purkis, B. R. Smith, R. Taylor, R. I. Cooper, S. E. Harris, A. G. Orpen, Retrieval of Crystallographically-Derived Molecular Geometry Information, J. Chem. Inf. Comput. Sci. 44 (2004) 2133–2144.

[21] F. H. Allen, The Cambridge Structural Database: a quarter of a million crystal structures and rising, Acta Crystallogr. B 58 (2002) 380–388.

[22] W. Koch, M. C. Holthausen, A Chemist's Guide to Density Functional Theory, Wiley-VCH, 2001.

[23] D. S. Sholl, J. A. Steckel, Density Functional Theory. A Practical Introduction, John Wiley & Sons, Inc., 2009.

[24] J. P. Perdew, A. Ruzsinszky, L. A. Constantin, J. Sun, G. I. Csonka, Some fundamental issues in ground-state density functional theory: A guide for the perplexed, J. Chem. Theory Comput. 5 (2009) 902–908.

[25] C. Lee, W. Yang, R. G. Parr, Development of the Colle-Salvetti correlation-energy formula into a functional of the electron density, Phys. Rev. B 37 (1988) 785–789.

[26] Jaguar, version 7.6, Schrödinger, LLC, New York, NY, 2009.

[27] J. Janak, Proof that $\partial E/\partial n_i = \varepsilon_i$ in density-functional theory, Phys. Rev. 1978 (18) 7165–7168.

[28] C.-G. Zhan, J. A. Nichols, D. A. Dixon, Ionization potential, electron affinity, electronegativity, hardness, and electron excitation energy: Molecular properties from density functional theory orbital energies, J. Phys. Chem. A 107 (2003) 4184–4195.

[29] R. G. Parr, L. V. Szentpály, S. Liu, Electrophilicity index, J. Am. Chem. Soc. 121 (1999) 1922–1924.

[30] QikProp, version 3.2, Schrödinger, LLC, New York, NY (2009).

[31] R. Martin, Electronic Structure: Basic Theory and Practical Methods, Cambridge University Press, 2004.

[32] J. D. Dunitz, X-Ray Analysis and the Structure of Organic Molecules, Wiley-VCH, 1992.

[33] E. Kaxiras, Atomic and Electronic Structure of Solids, Cambridge University Press, 2003.

[34] M. Dion, H. Rydberg, E. Schröder, D. Langreth, B. Lundqvist, Van der Waals density functional for general geometries, Phys. Rev. Lett. 92 (2004) 246401.

[35] G. Román-Pérez, J. M. Soler, Efficient implementation of a van der Waals density functional: Application to double-wall carbon nanotubes, Phys. Rev. Lett. 103 (2009) 096102.

[36] J. Klimeš, D. R. Bowler, A. Michaelides, Chemical accuracy for the van der Waals density functional, J. Phys. Condens. Matter 22 (2010) 022201.

[37] K. Lee, Éamonn D. Murray, L. Kong, B. I. Lundqvist, D. C. Langreth, Higher-accuracy van der Waals density functional, Phys. Rev. B 82 (2010) 081101.

[38] J. F. Dobson, T. Gould, Calculation of dispersion energies, J. Phys.: Condens. Matter 24 (2012) 073201.

[39] D.-L. Chen, W. A. Al-Saidi, J. K. Johnson, The role of van der Waals interactions in the adsorption of noble gases on metal surfaces, J. Phys.: Condens. Matter 24 (2012) 424211.

[40] J. Soler, E. Artacho, J. Gale, A. García, J. Junquera, P. Ordejón, D. Sánchez-Portal, The SIESTA method for ab-initio order-N materials simulation, J. Phys. Condens. Matter 14 (2002) 2745–2779.

[41] N. Troullier, J. L. Martins, Efficient pseudopotencials for plane-wave calculation, Phys. Rev. B 43 (1991) 1993–2006.

[42] E. Artacho, D. Sánchez-Portal, P. Ordejón, A. García, J. Soler, Linear-scaling ab-initio calculations for large and complex systems, Phys. Stat. Sol. (b) 215 (1999) 809–817.

[43] H. Monkhorst, J. Pack, Special points for Brillouin-zone integrations, Phys. Rev. B 13 (12) (1976) 5188–5192.

[44] M. A. Spackman, D. Jayatilaka, Hirshfeld surface analysis, Cryst. Eng. Comm. 11 (2009) 19–32.

[45] M. A. Spackman, J. J. McKinnon, Fingerprinting intermolecular interactions in molecular crystals, Cryst. Eng. Comm. 4 (2002) 378–392.

[46] J. J. McKinnon, M. A. Spackman, A. S. Mitchell, Novel tools for visualizing and exploring intermolecular interactions in molecular crystals, Acta Crystallogr. B 60 (2004) 627–668.

[47] M. A. Spackman, Molecules in crystals, Phys. Scr. 87 (2013) 048103.

[48] J. J. McKinnon, D. Jayatilaka, M. A. Spackman, Towards quantitative analysis of intermolecular interactions with Hirshfeld surfaces, Chem. Commun. 37 (2007) 3814–3816.

[49] A. P. Scott, L. Radom, Harmonic vibrational frequencies: An evaluation of Hartree-Fock, Moller-Plesset, quadratic configuration interaction, density functional theory, and semiempirical scale factors, J. Phys. Chem. 100 (1996) 16502–16513.

[50] M. L. Laury, M. J. Carlson, A. K. Wilson, Vibrational frequency scale factors for density functional theory and the polarization consistent basis sets, J. Comp. Chem. 30 (2012) 2380–2387.

[51] Torsten Schwede, Manuel C. Peitsch (Eds.), Computational Structural Biology. Methods and Applications, World Scientific, 2008.

[52] C. A. Lipinski, F. Lombardo, B. W. Dominy, P. J. Feeney, Experimental and computational approaches to estimate solubility and permeability in drug discovery and development settings, Adv. Drug Delivery Rev. 46 (2001) 3–26.

[53] W. L. Jorgensen, E. M. Duffy, Prediction of drug solubility from structure, Adv. Drug Delivery Rev. 54 (2002) 355–366.

[54] Maestro, version 11.1.011, Schrödinger, LLC, New York, NY (2017).

[55] R. G. Parr, R. G. Pearson, Absolute hardness: companion parameter to absolute electronegativity, J. Am. Chem. Soc. 105 (1983) 7512–7516.

[56] S. Wolff, D. Grimwood, J. McKinnon, M. Turner, D. Jayatilaka, M. Spackman, CrystalExplorer (Version 3.1), University of Western Australia (2012).

[57] R. Mulliken, Electronic population analysis on LCAO–MO molecular wave functions. I, J. Chem. Phys. 23 (1955) 1833–1840.

[58] R. Mulliken, Electronic population analysis on LCAO–MO molecular wave functions. II. Overlap populations, bond orders, and covalent bond energies, J. Chem. Phys. 23 (1955) 1841–1846.

[59] R. Mulliken, Electronic population analysis on LCAO-MO molecular wave functions. III. Effects of hybridization on overlap and gross AO populations, J. Chem. Phys. 23 (1955) 2338–2342.

[60] R. Mulliken, Electronic population analysis on LCAO-MO molecular wave functions. IV. Bonding and antibonding in LCAO and valence-bond theories, J. Chem. Phys. 23 (1955) 2343–2346.

[61] A. E. Reed, R. B. Weinstock, F. Weinhold, Natural population analysis, J. Chem. Phys. 83 (1985) 735–746.

[62] C. M. Breneman, K. B. Wiberg, Determining atom-centered monopoles from molecular electrostatic potentials. The need for high sampling density in formamide conformational analysis, J. Comp. Chem. 11 (1990) 361–373.

[63] U. C. Singh, P. A. Kollman, An approach to computing electrostatic charges for molecules, J. Comp. Chem. 5 (1984) 129–145.

[64] B. H. Besler, K. M. Merz, P. A. Kollman, Atomic charges derived from semiempirical methods, J. Comp. Chem. 11 (1990) 431–439.

[65] R. F. W. Bader, Atoms in Molecules: A Quantum Theory, Clarendon Press, 1994.

[66] G. Henkelman, A. Arnaldsson, H. Jónsson, A fast and robust algorithm for Bader decomposition of charge density, Comput. Mater. Sci. 36 (2006) 354–360.

[67] E. Sanville, S. Kenny, R. Smith, G. Henkelman, An improved grid-based algorithm for Bader charge allocation, J. Comp. Chem. 28 (2007) 899–908.

[68] W. Tang, E. Sanville, G. Henkelman, A grid-based Bader analysis algorithm without lattice bias, J. Phys.: Condens. Matter 21 (2009) 084204.

[69] F. M. Bickelhaup, N. J. R. van Eikema Hommes, C. F. Guerra, E. J. Baerends, The carbon–lithium electron pair bond in $(CH\_3Li)\_n$ (n = 1, 2, 4), Organometallics 15 (1996) 2923–2931.

[70] C. F. Guerra, J. W. Handgraaf, E. J. Baerends, F. M. Bickelhaupt, Voronoi deformation density (VDD) charges: Assessment of the Mulliken, Bader, Hirshfeld, Weinhold, and VDD methods for charge analysis, J. Comp. Chem. 25 (2004) 189–210.

[71] F. L. Hirshfeld, Bonded-atom fragments for describing molecular charge densities, Theor. Chim. Acta 44 (1977) 129–138.

[72] F. Martin, H. Zipse, Charge distribution in the water molecule. A comparison of methods, J. Comput. Chem. 26 (2005) 97–105.

[73] C. Giacovazzo, H. L. Monaco, G. Artioli, D. Viterbo, M. Milanesio, G. Gilli, P. Gilli, G. Zanotti, G. Ferraris, Fundamentals of crystallography, Oxford University Press, 1992.

[74] M. Donahue, E. Botonjic-Sehic, D. Wells, C. W. Brown, Understanding infrared and raman spectra of pharmaceutical polymorphs, Am. Pharmaceut. Rev. 14 (2011) 1.

[75] F. Weinhold, C. R. Landis, Discovering chemistry with natural bond orbitals, John Wiley & Sons, Inc., Hoboken, New Jersey, 2012.

[76] F. Weinhold, E. D. Glendening, NBO 6.0 Program Manual. Natural Bond Orbital Analysis Programs (2013).

Research Highlights

Paper: "*Synthesis, characterization and theoretical study in gaseous and solid phases of the imine 4-Acetyl-N-(4-methoxybenzylidene)aniline*"

Authors: J.F.N. Batista, J.W. Cruz Jr., A.C. Doriguetto, C. Torres, E.T. de Almeida and I. Camps

Journal: Journal Molecular Structure

- The calculated chemical descriptors indicates an electronically stable molecule.
- Title compound has pharmacological drug like properties.
- Solid phase of title compound is a low gap semiconductor.
- Carbon and oxygen atoms contribute must to HOMO/LUMO and electronic bands.